processes

MDPI

Article

Functional Improvement of NiO_x/CeO_2 Model Catalyst Active in Dry Methane Reforming via Optimization of Nickel Content

Piotr Legutko [1,*], Mateusz Marzec [2], Marcin Kozieł [1], Krystian Sokołowski [2], Marek Michalik [3] and Andrzej Adamski [1]

[1] Faculty of Chemistry, Jagiellonian University, Gronostajowa 2, 30-387 Kraków, Poland; marcin.koziel@uj.edu.pl (M.K.); a.adamski@uj.edu.pl (A.A.)
[2] Academic Centre for Materials and Nanotechnology, AGH University of Krakow, Mickiewicza Avenue 30, 30-059 Kraków, Poland; marzecm@agh.edu.pl (M.M.); krysok@agh.edu.pl (K.S.)
[3] Institute of Geological Science, Jagiellonian University, Gronostajowa 3a, 30-387 Kraków, Poland; marek.michalik@uj.edu.pl
* Correspondence: piotr.legutko@uj.edu.pl; Tel.: +48-686-2571

Abstract: The valorization of greenhouse gases, especially when focused on carbon dioxide, currently belongs to the main challenges of pro-environmental chemical processes. One of the important technologies in this field is dry methane reforming (DMR), leading to the so-called synthesis gas ($CO + H_2$). However, to be efficient and economically viable, an active and stable catalyst is required. Ni-based systems can be recommended in this regard. This research aimed to investigate how nickel content can influence the activity of model NiO_x/CeO_2 catalysts in DMR. A series of NiO_x/CeO_2 samples of various nickel loadings (0–10 wt.%) were prepared through dry impregnation. The obtained samples were characterized through XRD, RS, N_2-BET, DRIFT, SEM, UV/Vis-DR, and XPS. Nonlinear changes in surface properties of the investigated samples with increasing nickel concentration were found. The observed changes are mirrored both in the determined nickel speciation and in the corresponding catalytic activity. The highest activity was found for the catalyst containing 3 wt.%. of nickel.

Keywords: dry methane reforming; ceria-supported nickel catalysts; the effect of concentration; surface structure

Citation: Legutko, P.; Marzec, M.; Kozieł, M.; Sokołowski, K.; Michalik, M.; Adamski, A. Functional Improvement of NiO_x/CeO_2 Model Catalyst Active in Dry Methane Reforming via Optimization of Nickel Content. *Processes* **2024**, *12*, 851. https://doi.org/10.3390/pr12050851

Academic Editor: Hsin Chu

Received: 29 March 2024
Revised: 19 April 2024
Accepted: 22 April 2024
Published: 23 April 2024

1. Introduction

Over the last 100 years, energy consumption has rapidly grown as the world population has skyrocketed, and technological and economic progress have significantly intensified. Moreover, the common use of cars and planes along with engine-powered trains and ships has made us extremely dependent on hydrocarbon-based fuels, such as gasoline, diesel, and jet fuels. The combustion of solid, liquid, and gaseous fossil fuels in various mobile and stationary energy-generated systems entails many environmental problems, including those related to the emission of greenhouse gases (GHGs). An increase in global environmental awareness boosted a common trend to reduce the emission of GHGs, especially CO_2 [1–3].

One of the most interesting technological ideas of CO_2 utilization is its conversion into a mixture of hydrogen and carbon monoxide, commonly called synthesis gas. This concept was originally described in 1928 by F. Fischer and H. Tropsch, who proposed various transition metals as catalysts, including Ni- and Co-based systems [4]. Synthesis gas can be obtained in the reaction (1) described in the literature as dry reforming of methane (DMR):

$$CH_{4(g)} + CO_{2(g)} = 2CO_{(g)} + 2H_{2(g)}, \quad (1)$$

Due to quite demanding process conditions, there was no technological interest in the industrial implementation of this process for several decades, but, nowadays, environmental reasons and stricter regulations imposed on emitters make methane reforming

attention-grabbing. This is because in the DMR reaction, two greenhouse gases (i.e., CO_2 and CH_4), constituting more than 90% of all GHGs emitted, are simultaneously converted into valuable products [3,5–7].

The DMR is a highly endothermic reaction with ΔH^0 = 247.3 kJ/mol and ΔG^0 = 66,170 − 67.32T, so a high temperature is required to gain a satisfactory conversion. The reaction is practically thermodynamically inhibited below 640 °C [5,6,8]. An additional challenge one must face in the case of DMR is reaction conditions because side reactions, like methane decomposition (2) (ΔH^0 = 75.6 kJ/mol)

$$CH_{4(g)} \rightarrow C_{(s)} + 2H_{2(g)}, \quad (2)$$

And the Boudouard reaction (3) (ΔH^0 = 172 kJ/mol)

$$2CO_{(g)} \rightarrow CO_{2(g)} + C_{(s)}, \quad (3)$$

may also occur [7,8]. They both result in carbon deposit formation, which is responsible for progressive blockage of active centers on the catalyst's surface by coking. Maximal coking is reported in the temperature range of 557–700 °C because methane decomposition occurs above 557 °C, whereas the Boudouard reaction is usually expected to occur below 700 °C.

Besides noble metals, great attention is paid to nickel deposited on various supports [9]. However, its resistance to carbon deposit formation is distinctly lower than that reported for noble metals [10]. There are several ways to improve nickel-based catalysts' stability for DMR. According to [11,12], there are three main routes to achieve more satisfactory resistance to the formation of carbon deposits: (i) the modification of the method of nickel introduction onto the catalyst support, (ii) the introduction of promoters or alloying metal additives, and (iii) the selection of appropriate supports.

An example of the optimization of the method of nickel introduction is so-called flame aerosol deposition [13]. It resulted in enhanced activity and stability in the DMR reaction. A similar method proposed in [14] was applied to obtain Ni/Al_2O_3. Moreover, it was shown that calcination temperature plays an important role in controlling the size of nickel particles and thus the activity and stability of the resulting catalytical systems. Moreover, partial coverage of nickel particles by semiconducting oxides, i.e., titania, was reported as a method to improve resistance to coking. However, this method led to simultaneous catalyst deactivation [15]. The formation of core–shell structures seems to be a promising way to synthesize DMR catalysts. Sandwiched $Ni\text{-}SiO_2@SiO_2$ catalysts are also an example of the successful employment of this method [16].

Another route is to add promoters or alloying metals to the parent Ni-based systems that can improve catalytic stability. An example of such a strategy can be the addition of iron to nickel/alumina–zirconia catalyst [17]. In the mentioned research, it was found that the addition of iron led to an increment in catalyst resistance to coking, as well as hydrogen yield. The addition of alkaline earth metals, like strontium, leads to the enhancement of basic properties of the surface of the Ni-based catalysts and thus inhibits coke formation [18]. A similar effect was observed in the case of alkali metals, and so cesium was added to $Ni/Al_2O_3\text{-}ZrO_2$ and optimized at the concentration level of 3 wt% of Cs [19]. Indium was added to a $Ni/CeO_2\text{-}Al_2O_3$ catalyst to form a NiIn alloy that resulted in enhanced stability due to nickel's stabilization in metallic form [20]. A trimetallic alloy of Ni-Pt-Co was immobilized on attapulgite-based zeolite supports. It was found that the Pt/Co ratio determined the catalytic performance of this system [21]. However, the addition of platinum to the Ni/CeO_2 catalyst facilitated the creation of defects, i.e., oxygen vacancies that resulted in the formation of active oxygen species' formation and thus enhanced catalytic properties in DMR [22].

The third strategy is the usage of appropriate supports, like mesoporous γ-alumina [23,24], zeolites (i.e., ZSM-5, BEA, MOR, USY) [25,26], perovskites, i.e., $LaAlO_3$ [27], and basic oxides, like MgO or CaO [28,29]. Especially interesting results were found for the systems based on ceria and/or zirconia [30–38]. What is rather surprising is that almost no or

relatively little attention was paid in the previously published papers to the effect of active metal concentration on its catalytic performance in DMR. In the literature devoted to dry methane reforming, only a few researchers have investigated this issue in more detail, as it can be inferred from the papers [39–43]. Despite this fact, it is clearly seen from the literature mentioned above that the loading of active metal may be decisive in obtaining a catalyst showing both high activity and satisfactory stability.

This work was focused on the investigation of the nickel loading effect on the structure and catalytic properties of a series of model NiO_x/CeO_2 catalysts for dry methane reforming. The reported results may constitute useful guidelines for the structural optimization of the supported Ni-based DMR catalysts.

2. Materials and Methods

The CeO_2 support was synthesized through the Pecchini method from cerium(III) nitrate hexahydrate (*Aldrich*, St. Louis, MO, USA), citric acid monohydrate (*POCh*, Gliwice, Poland), and ethylene glycol (*Fisher*, Hampton, NH, USA) in a molar ratio of 1:1.1:2. All reactants used for synthesis were of *per analysis* purity. Cerium(III) nitrate was dissolved in a minimal amount of water, and then citric acid was added to the mixture and the stirring was continued. After the total dissolving of citric acid, ethylene glycol was added. The resulting solution was mixed and heated on a magnetic stirrer until a gel was formed. The obtained residue was dried overnight at 120 °C and then calcined in air at 800 °C for 6 h. Final catalysts were prepared through impregnation of ceria support with aqueous solutions of nickel nitrate (*Sigma-Aldrich*, St. Louis, MO, USA) containing appropriate concentrations to obtain nickel contents in the final preparations ranging from 0 to 10 wt.%. A sample with nickel loading of x wt.% can be labeled hereafter as $x NiO_x/CeO_2$. After impregnation, all samples were dried overnight at 120 °C and then calcined at 400 °C in the air for 3 h to decompose the precursors. Such a procedure is similar to those applied in [44–46]. The NiO reference sample was synthesized through precipitation from a nickel(II) nitrate solution using a 25% aqueous solution of ammonia, filtered, dried overnight at 120 °C, and then calcined in air at 400 °C for 3 h.

The structure of the obtained samples was verified through X-ray diffraction (XRD). For data collection, a PANalytical (Malvern, UK) X'pert Pro diffractometer equipped with a PW3050/60 goniometer and CuKα lamp (λ = 1.5406 Å) was used. The anode voltage was set to 40 kV, while the anode current was set to 30 mA. The diffraction patterns were measured from 10° to 90° with a step of 0.026°. The size of crystallites was estimated based on the Scherrer equation [47]:

$$d_{XRD} = \frac{K \times \lambda}{\beta \times \cos\theta}, \quad (4)$$

where K is a dimensionless shape factor (0.93); λ is the X-ray wavelength (0.15406 nm); β is the line broadening at half the maximum intensity (FWHM); and θ is the Bragg angle. Further studies of the structure were performed through micro-Raman spectroscopy. A Renishaw (Wotton-under-Edge, UK) InVia spectrometer equipped with a Leica DMLM confocal microscope and a CCD detector, with an excitation wavelength of 785 nm, was used to record RS spectra under ambient conditions. The power of the laser was 1.5 mW (0.5% of the total power) with a magnification of 20 times. Data collection was performed in the range of 150 to 800 cm^{-1}. At least 9 scans (15 s each) were recorded.

The Brunauer–Emmett–Teller (BET) method was applied for the surface area measurements of the investigated samples. To do so, 3Flex chemisorption by Micrometrics (Unterschleißheim, Germany) using nitrogen adsorption (−196 °C) was used for the measurements. The mean particle size estimated from BET (d_{BET}) was calculated from the Equation (5):

$$d_{BET} = \frac{6000}{\rho S_{BET}}, \quad (5)$$

where ρ is the theoretical density of CeO_2 and S_{BET} is the surface area estimated by the BET method [48]. A JEOL (Peabody, MA, USA) FEG 6700F microscope working at 9 kV accelerating voltage was employed for scanning electron microscopy (SEM) images.

A *Bruker* (Billerica, MA, USA) Tensor 27 spectrometer equipped with a *Specac* (Orpington, UK) DRIFT Environmental Chamber, a temperature controlling unit, and a He-Ne laser (λ = 633 nm) was used to collect Diffuse Reflectance Fourier Transform IR (DRIFT) spectra. The measurements were performed in a vacuum (10^{-6} bar) in the frequency range of 4000–600 cm^{-1} with a resolution of 2 cm^{-1}. Each spectrum was measured with 256 accumulations to obtain sufficiently intense spectra. Nickel speciation was investigated through UV/Vis diffuse reflectance spectroscopy employing a Perkin-Elmer (Waltham, MA, USA) Lambda 650 UV/Vis spectrophotometer with Praying Mantis (Harrick, Pleasantville, NY, USA). Each spectrum was recorded in the range of 200–900 nm with a resolution of 1 nm under ambient conditions, and the data were transformed according to the Kubelka–Munk equation. Deconvolution of the spectra was carried out using the Fityk software (v.0.8.0).

X-ray photoelectron spectroscopy (XPS) was employed for further surface investigation. The XPS system *PHI* (Lake Drive East Chanhassen, MN, USA) VersaProbeII was used for data collection. This scanning XPS system uses monochromatic Al K_α (1486.6 eV) X-rays focused on a 100 μm spot. The scan is performed over the sample area of 400 μm × 400 μm. The photoelectron take-off angle was set to 45°, and the pass energy in the analyzer was set to 23.50 eV to obtain high-energy resolution spectra for the C 1s, O 1s, Ni 2p, and Ce 3d regions. To maintain a constant sample surface potential regardless of the sample conductivity, a dual beam charge compensation with 7 eV Ar^+ ions and 1 eV electrons was used. The C1s' peak of unfunctionalized, saturated carbon (C-C) at 284.8 eV was used to charge-reference all XPS spectra. The pressure in the analytical chamber was below $4{\cdot}10^{-9}$ mbar. *PHI* MultiPak software (v.9.7.0.1) was employed for the deconvolution of spectra. The Shirley method was used for spectrum background subtraction.

Catalytic activity in DMR was measured as follows: a mixture of gases with a total flow of 100 mL/min (5% CO_2/He = 50 mL/min, 5% CH_4/He = 50 mL/min) was introduced into a quartz reactor containing 100 mg of a catalyst. Reagents were analyzed using a gas chromatograph (Agilent Technologies, Santa Clara, CA, USA, 7890A GC System). In the first step, a catalyst was reduced at 850 °C with 5% H_2/Ar flow (50 mL/min) for 120 min. After reaching a temperature of *ca.* 550 °C, the H_2 flow was switched off, and other gaseous reactants were turned on. Gas chromatographic measurements were performed from 600 °C every 50 °C up to 800 °C and one back at 650 °C. The conversion of CO_2 and CH_4, as well as the H_2/CO ratio, were calculated by comparing the concentrations of these reactants before and after the catalytic reactor, similarly to [49–51].

3. Results and Discussion

3.1. Structural Characterization

As it can be seen in Figure 1a, the structure of the synthesized CeO_2 support was crystalline, giving rise to a regular phase with characteristic Bragg reflections (JCPDS card no. 34-0394), and its impregnation with aqueous solutions of nickel(II) nitrate of various concentrations followed by calcination at 400 °C did not influence the phase composition of the studied support. The average size of the support crystallites estimated using the Scherer method was *ca.* 43 nm. The lack of a broadening visible in the recorded XRD patterns suggested that independently of its nominal content, nickel was not incorporated into the bulk of CeO_2 and formed separate surface entities, which can be identified as NiO nanocrystals (JCPDS Card No. 00-004-0835), giving rise to the maxima at 37.2°, 43.3°, and 63.2° (more visible in Figure 1b), attributed to (021), (202), and (024), respectively, which are reflections characteristic of nickel(II) oxide. They can be observed in the XRD patterns recorded for samples containing more than 3 wt.% of nickel, and their intensity increased with nickel loading.

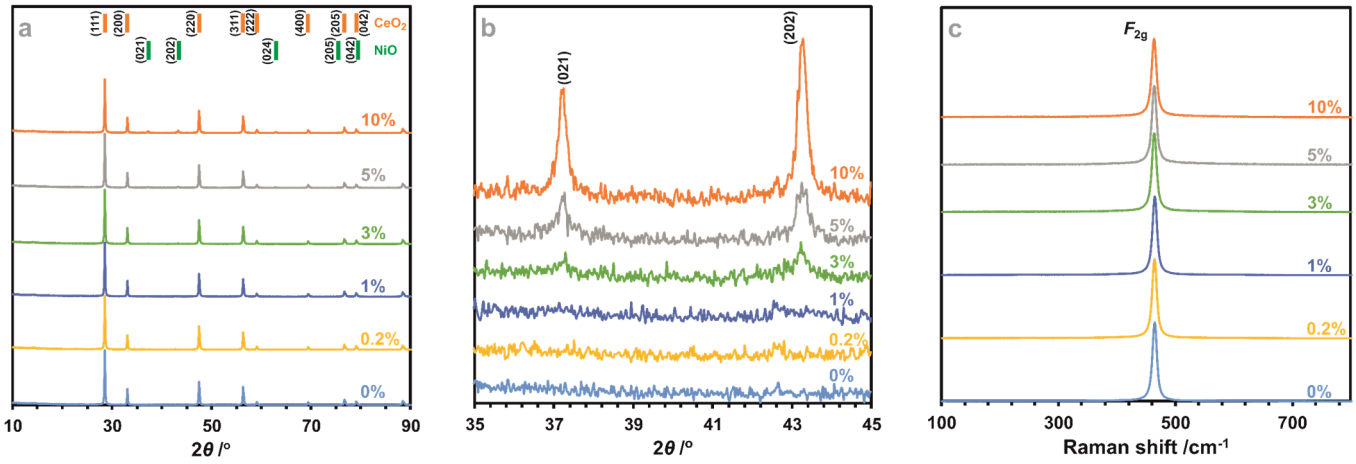

Figure 1. Diffraction patterns (**a**) and their zooming in the range of 35–45° (**b**), and Raman spectra (**c**) of the studied NiO_x/CeO_2 samples of various concentrations of nickel (from 0 to 10 wt. %).

Any changes in the recorded Raman spectra as a consequence of nickel deposition on ceria cannot be identified (Figure 1c). Only an intense band at about 460 cm^{-1}, attributed to the characteristic vibrations of F_{2g} symmetry in the CeO_2 regular phase [52], dominated in all recorded spectra. The lack of a broad band at *ca.* 590 cm^{-1}, usually attributed to the vibrations associated with oxygen vacancies induced in the ceria structure by nickel incorporation [53], suggested that nickel was stabilized mainly on the surface. That remains in agreement with the XRD results reported previously. Bulk NiO was not detected through Raman spectroscopy, which can be explained by a good dispersion as a possible result of relatively strong interactions between the active phase and the support [53].

3.2. Morphology

The specific surface of CeO_2 support determined through the N_2-BET method was found to be rather low and equal to 5.37 m^2/g. It slightly increased after the deposition of nickel to reach specific surface areas (SSA), from 6.02 m^2/g for $3NiO_x/CeO_2$ to 8.42 m^2/g for $10NiO_x/CeO_2$. Partial segregation of the NiO phase at the highest loading is thus possible. The particle sizes of the investigated samples estimated based on the BET results were distinctly higher than those attributed to crystallites of diameters determined based on the XRD results (155 nm from BET and 42 nm from Scherrer for CeO_2). This suggests that one particle was built from around 60 crystallites. Although all surface areas reported for the investigated supported samples increased with growing nickel contents, their micropore areas changed in a rather nonlinear way. As such, the micropores took 30% of the CeO_2 support area (1.60 m^2/g) and 15% of the area in the case of the $10NiO_x/CeO_2$ sample (1.30 m^2/g), whereas they took only 11% of $3NiO_x/CeO_2$ area (0.66 m^2/g). At the same time, the external surface areas consequently increased from 3.77 m^2/g (for CeO_2) to 5.35 m^2/g (for $3NiO_x/CeO_2$) to 7.12 m^2/g (for $10NiO_x/CeO_2$). Based on that, it can be stated that during impregnation, some of the pores became partially filled, and the segregation of NiO led to an increment in the surface area and was responsible for the formation of new pores within NiO nanocrystals. In any case, the volume of the micropores was relatively low and equal to 0.00103 cm^3/g (for CeO_2), 0.00036 cm^3/g (for $3NiO_x/CeO_2$), and 0.00046 cm^3/g (for $10NiO_x/CeO_2$). This remains in agreement with Figure 2, in which only narrow hystereses on the type V isotherms can be observed [54].

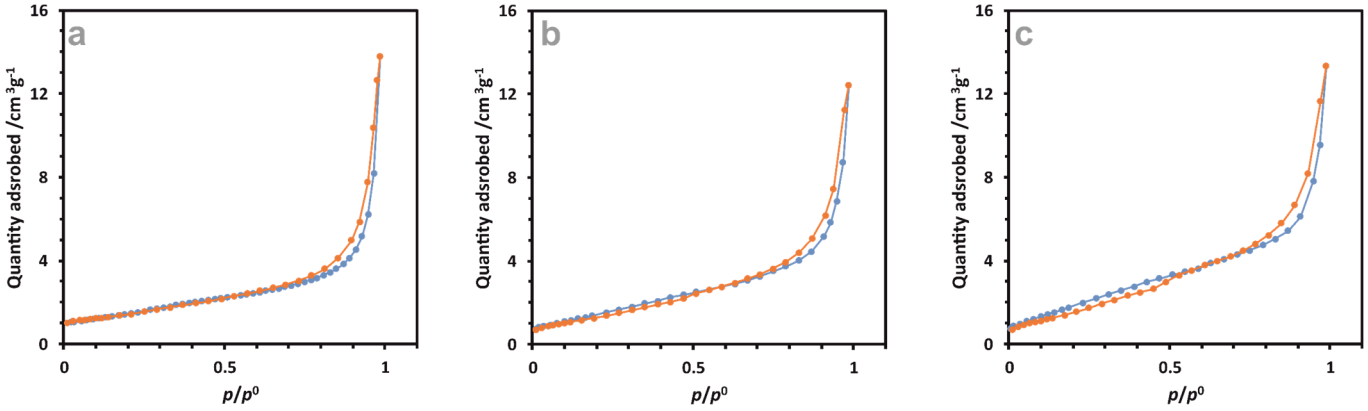

Figure 2. The N_2 adsorption/desorption isotherms measured for CeO_2 (**a**), $3NiO_x/CeO_2$ (**b**), and $10NiO_x/CeO_2$ (**c**).

SEM images (Figure 3) of the investigated catalysts showed a wide range of grain sizes. Generally, grain diameters measured just a few micrometers; however, larger aggregates with dimensions higher than 20 µm were also observed. Any notable changes with increasing nickel loading can be observed.

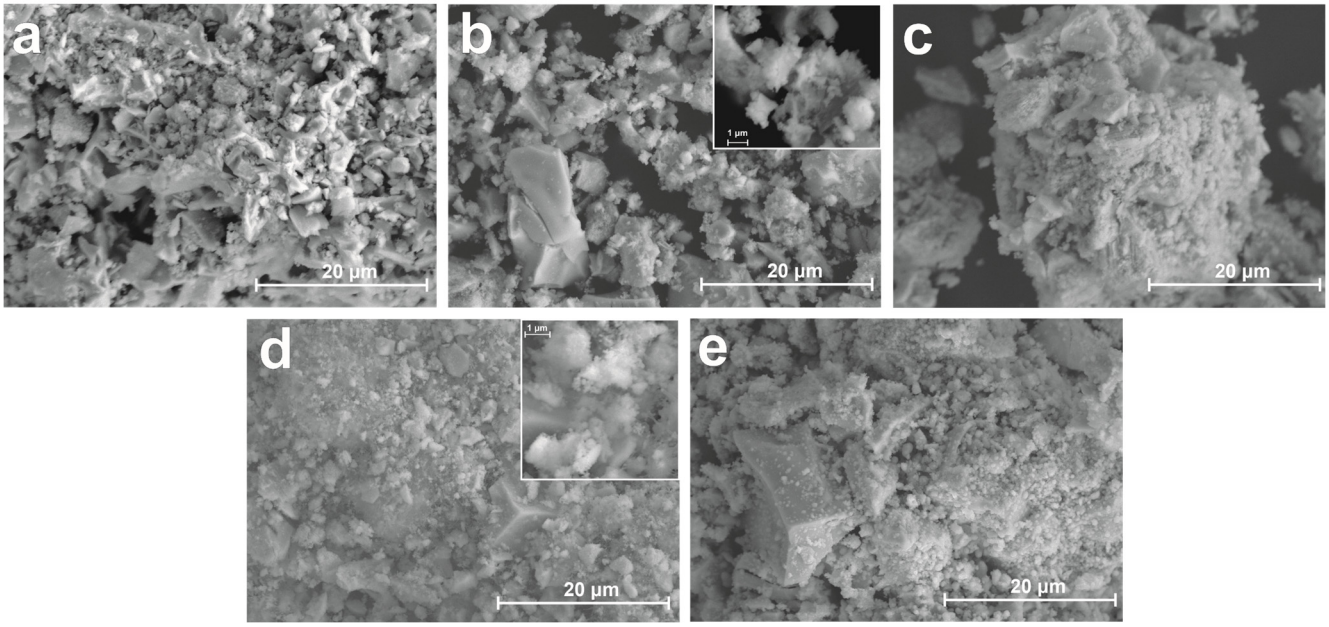

Figure 3. Scanning electron microscopic images of the fresh catalysts $0.2NiO_x/CeO_2$ (**a**), $1NiO_x/CeO_2$ (**b**), $3NiO_x/CeO_2$ (**c**), $5NiO_x/CeO_2$ (**d**), and $10NiO_x/CeO_2$ (**e**). The inserts with higher magnification are added for selected samples.

3.3. Surface Characterization

The analysis of hydroxyls that presented on the surface of the investigated samples can be seen in Figure 4. Regarding CeO_2 support, four hydroxyl bands can be detected: a single bonded hydroxyl group (type I) as a shoulder around 3700 cm^{-1} and two types of hydroxyls bicoordinated (type IIA) to Ce(III) centered at 3690 cm^{-1} and Ce(IV) centered at 3655 cm^{-1}. The last peak can be ascribed to hydroxyl coordinated to two cations localized in the vicinity of an oxygen vacancy (type IIB) to Ce(IV) centered at 3620 cm^{-1} [55,56]. It is noteworthy that even small amounts of nickel led to the disappearance of the bands attributed to hydroxyl groups mentioned above, with the simultaneous appearance of the band at 3680 cm^{-1}, which is typical of hydroxyls bonded to nickel(II) centers. Such an

interpretation was confirmed by our reference DRIFT measurement carried out for the NiO sample as well as by data from the literature [57]. A similar situation can be observed in the case of carboxyl groups from adsorbed CO_2 from the air. Some of the bands visible in the DRIFT spectra of bare CeO_2 disappeared even at small nickel loading. Instead of carboxyl groups bonded to cerium centers, the doublet band at 1275–1260 cm^{-1} appeared, which can be ascribed to the vibration of the C-O bond [57]. Those DRIFT results partially confirm strong interactions between CeO_2 support and the nickel-containing deposited phase. Additionally, the heterogeneity of surface hydroxylation has been confirmed.

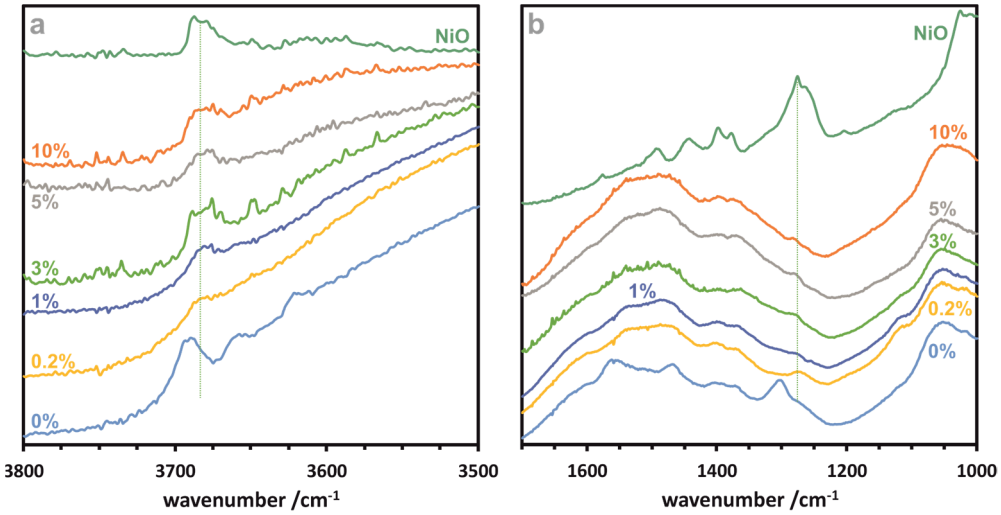

Figure 4. DRIFT spectra of the investigated samples in the diagnostic hydroxyl (**a**) and structural and carboxyl (**b**) regions.

Deconvoluted UV/Vis-DR spectra recorded for both CeO_2 and NiO_x/CeO_2 samples in ambient conditions are shown in Figure 5. The spectrum of CeO_2 support (Figure 5a) was deconvoluted into three peaks with maxima at 221, 276, and 343 nm. The first maximum can be attributed to the ligand-to-metal charge transfer (LMCT) $O^{2-} \rightarrow Ce^{3+}$ transitions, while the second, LMCT $O^{2-} \rightarrow Ce^{4+}$ transitions, and the last one—to the interband transitions [58,59]. The addition of a small amount of nickel (0.2%) resulted in a UV/Vis-DR spectrum quite similar to the spectrum of the undoped sample (Figure 5b). Moreover, an expanded broad band at higher wavelengths can be easily visible. The presence of this kind of band can be attributed to the transition characteristic of bulk NiO [60]. A further increase in nickel loading led to the increment of the intensity of the bands characteristic of nickel oxides (Figure 5c–f).

The surface analysis performed using XPS in the characteristic Ni 2p region (Figure 6a) showed that both metallic and oxidized nickel coexisted on the surface of all the impregnated samples, while Ni^{2+} was stabilized in the form of hydroxide $Ni(OH)_2$ and oxyhydroxide NiOOH, as it can be inferred from the spectra after the fitting procedure [61]. The ratio of metallic nickel species to the oxidized one depended on nickel loadings. This ratio as a function of nickel concentration changed in a nonlinear way (Figure 6c). The analysis of the Ce 3d region (Figure 6b) showed that both Ce^{3+} and Ce^{4+} were present on the surface of all investigated samples. The Ce^{3+}/Ce^{4+} concentration ratio apparently changed with nickel loading (Figure 6d)—a fast decrement in this ratio can be observed up to 1 wt.% of nickel, and, above this value, the observed changes were smaller.

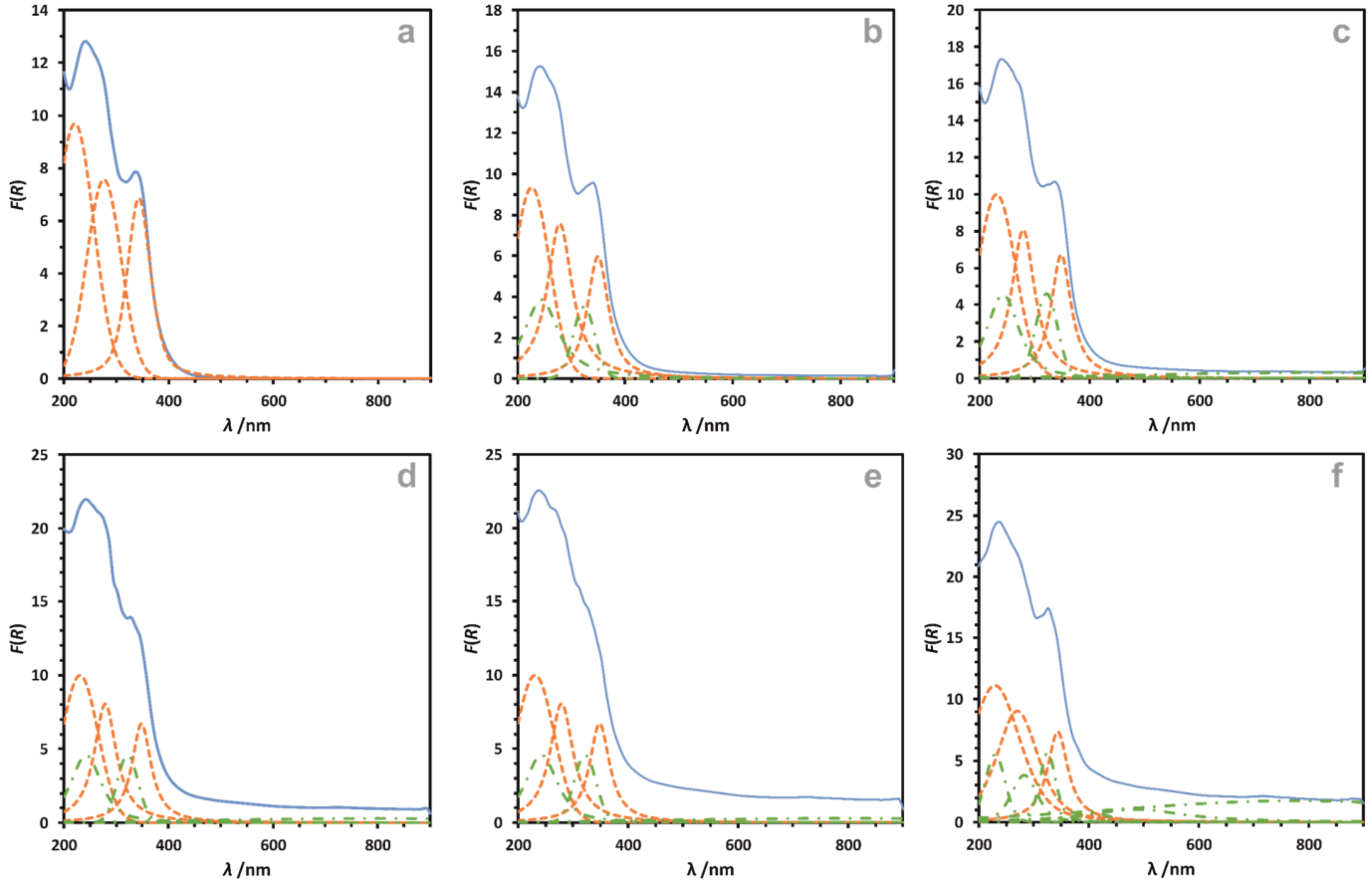

Figure 5. Deconvoluted UV/Vis-DR spectra of the studied NiO_x/CeO_2 samples of various concentrations of nickel: 0 wt. % (**a**), 0.2 wt. % (**b**), 1 wt. % (**c**), 3 wt. % (**d**), 5 wt. % (**e**), and 10 wt. % (**f**). Orange dashed line—peaks characteristic of CeO_2 absorption; green dotted–dashed line—peaks characteristic of NiO absorption.

The overall surface composition of the investigated samples is collected in Table 1. As it can be seen, the concentrations of nickel were higher than the nominal value, which was expected due to the manner of its introduction—impregnated samples tend to localize nickel on the surface rather than in the bulk. However, the observed increment in the surface concentrations of nickel as a function of its nominal value is asymptotic, which suggests that nickel can be partially incorporated into the subsurface layers or, what is more probable, at higher loadings, nickel formed bigger crystals with higher loading (which remains in agreement with the reported XRD results). The cerium concentration decreased with nickel loading. This observation most probably suggests that cerium was covered by nickel on the surface. The concentration of oxygen remained constant in the investigated range.

Table 1. Surface compositions of the investigated samples through XPS.

Sample	Ni/at. %	Ce/at. %	O/at. %
CeO_2	-	18	82
$0.2NiO_x/CeO_2$	2.1	18	80
$1NiO_x/CeO_2$	3.8	16	80
$3NiO_x/CeO_2$	4.7	16	79
$5NiO_x/CeO_2$	6.1	15	79
$10NiO_x/CeO_2$	6.3	13	81

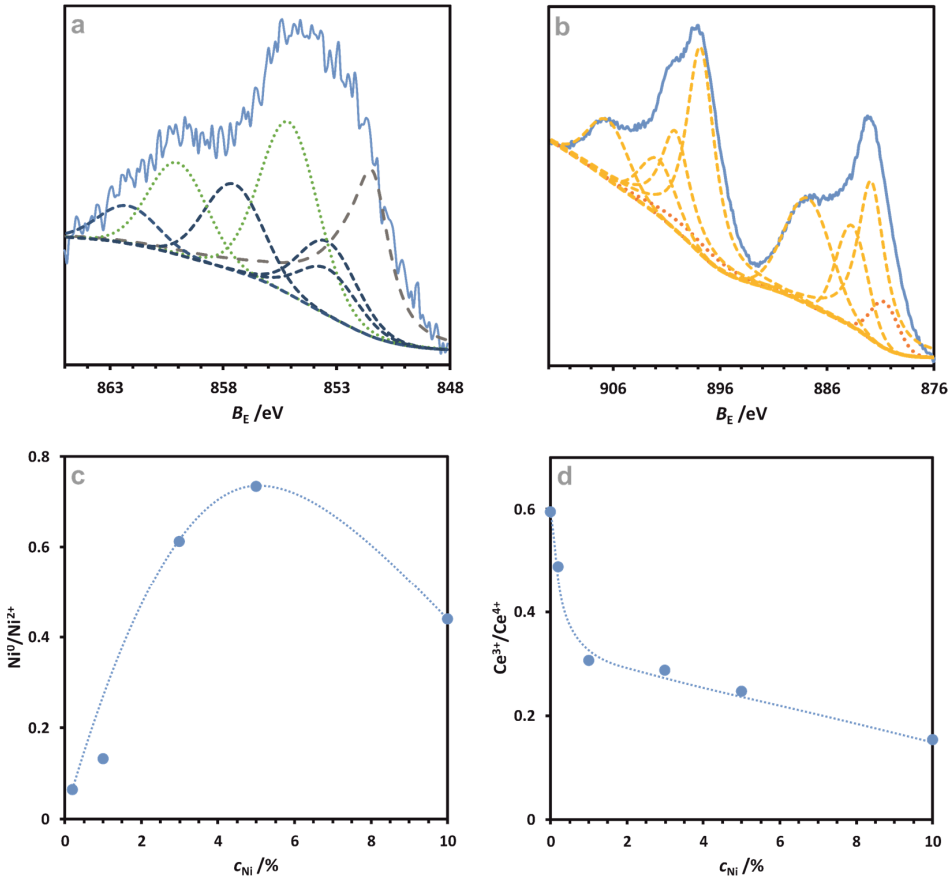

Figure 6. High-resolution XPS analysis of Ni 2p (**a**) and Ce 3d regions (**b**) of $3NiO_x/CeO_2$ catalyst, together with the determined Ni(0)/Ni(2+) ratio (**c**) and Ce(3+)/Ce(4+) ratio (**d**) as a function of nickel loading.

3.4. Catalytic Activity

At temperatures above 550 °C, all NiO_x/CeO_2 samples containing at least 1 wt. % of nickel showed catalytic activity in dry methane reforming at temperatures above 550 °C. The observed catalytic conversions generally increased with temperature (Figure 7a,b). However, a rapid deactivation was observed for the catalyst of the highest (10 wt.%) investigated loading of nickel. This can be explained by the formation of larger aggregates of nickel species, which is adverse to activity because of a higher amount of hidden nickel inside those aggregates. In this case, the conversion of CO_2 was higher than the corresponding conversion of CH_4 (maximal values above 90% and 60%, respectively). This effect can be explained by the associated occurrence of the reverse water–gas shift reaction (RWGS) (6)

$$H_{2(g)} + CO_{2(g)} = CO_{(g)} + H_2O_{(g)}, \quad (6)$$

which is the main side reaction competing with DMR. As a result of RWGS, the maximal ratio of the DMR products, hydrogen and carbon monoxide, was slightly lower than the stoichiometric ratio, i.e., it remained below unity for all investigated catalysts. Generally, the H_2/CO concentration ratio seems to be somehow associated with the activity of the investigated catalysts. As it was confirmed by the current studies, both vital catalytic parameters, i.e., activity and selectivity, nonlinearly depend on nickel loading (Figure 7d–f). Maximal values of the activity were observed for 3 wt.% of nickel content, suggesting that the vital concentration-dependent factors (degree of Ni reduction, active-phase dispersion, as well as nickel speciation) are the crucial parameters for activity in dry methane reforming. Moreover, those parameters can be controlled by the appropriate optimization of nickel loading. Similar results were found for Ni/Al_2O_3-CeO_2 catalysts, where the influence

of nickel loading was investigated in the range of 2.5 wt% to 15 wt% and the optimal concentration was found for 10 wt of Ni [62].

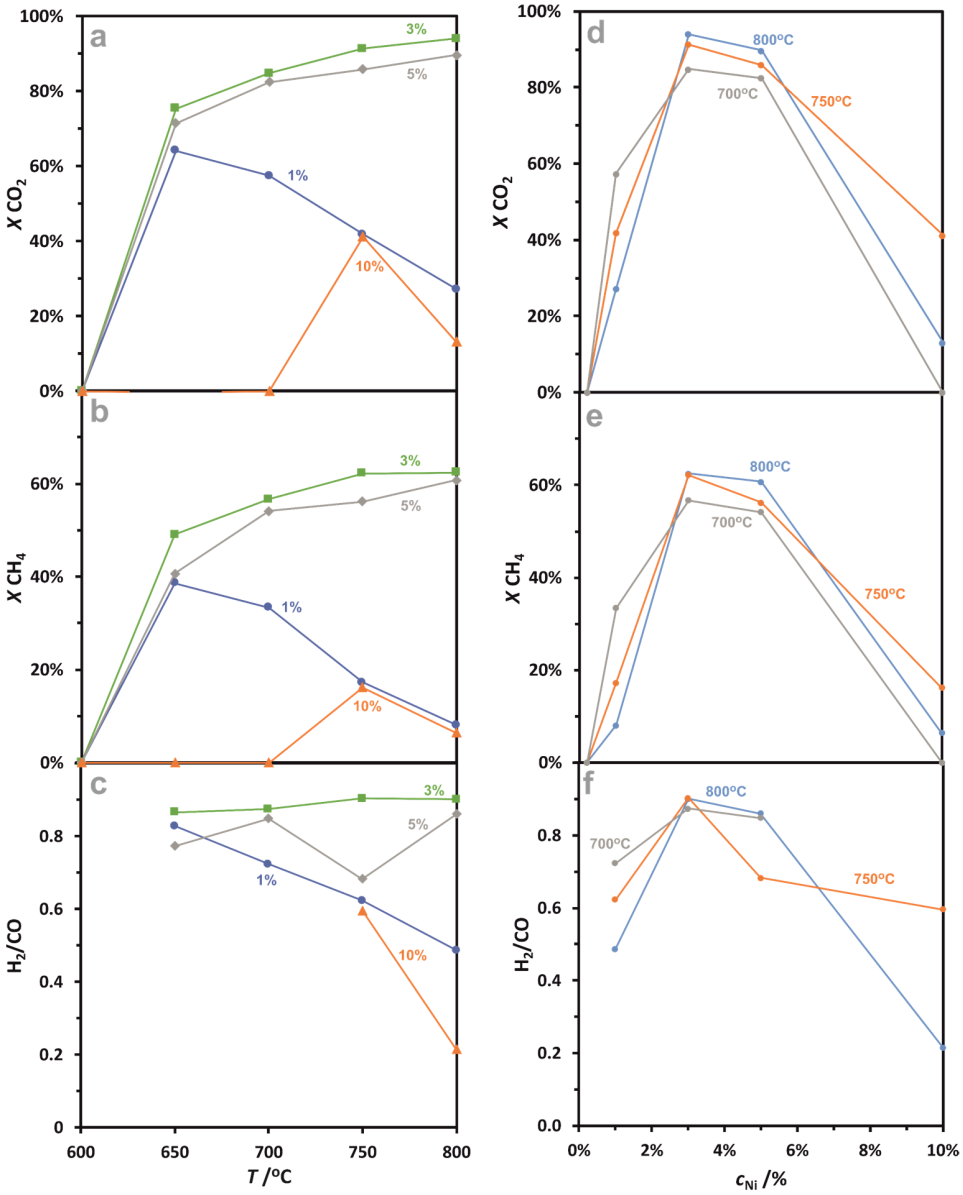

Figure 7. Conversion of CO_2 (**a**) and CH_4 (**b**) together with H_2/CO (**c**) product content ratio as a function of temperature, as well as the conversion of CO_2 (**d**) and CH_4 (**e**) together with H_2/CO (**f**) product content ratio as a function of the nominal nickel concentration in the series of NiO_x/CeO_2 catalysts (1–10% Ni) tested in dry methane reforming.

An experiment to investigate the deactivation progress of the investigated catalysts required a return measurement of activity at 650 °C. A comparison of activity at the beginning of the catalytic test and after raising the reaction temperature to 800 °C is shown in Figure 8. It can be noticed that even if the optimal nickel concentration for DMR is 3 wt. %, taking into account the catalytic activity, the stability of the investigated catalysts distinctly increases with nickel loading, and thus the $5NiO_x/CeO_2$ catalyst showed better catalytic performance. The lower catalytic activity of $5NiO_x/CeO_2$ in comparison to $3NiO_x/CeO_2$ resulted in a lower rate of carbon deposit production and thus better stability. Moreover, the 5 wt.% sample possibly had a higher number of active centers (however, they were less active).

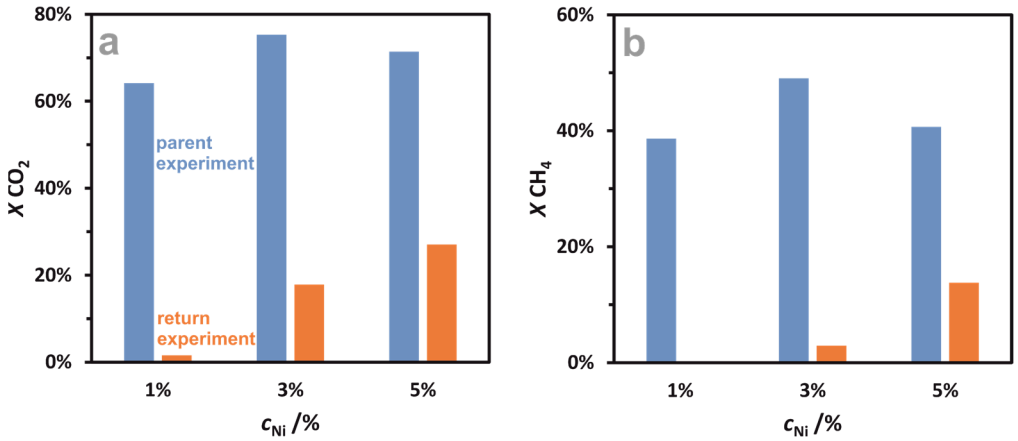

Figure 8. Conversion of CO_2 (**a**) and CH_4 (**b**) in 650 °C (initial and return (to the back point) experiments) for NiO_x/CeO_2 catalysts (1–5% Ni) tested in dry methane reforming.

SEM images of the investigated catalysts after the catalytic tests in DMR are shown in Figure 9. It can be stated that there are no significant changes in the grain morphology of supports; however, for the most active samples, 3% and 5% of nickel, characteristic carbon whiskers [63,64] can be observed. This clearly shows the reason for the observed activity decrement. Careful inspection of the images recorded at the higher magnification showed nickel/nickel oxide grains of diameters ranging several hundred nanometers. Such structures can be analyzed as a part of agglomerates/aggregates of dimensions from one to a few micrometers. Their formation can be a result of nickel reduction in the course of the DMR reaction. Images recorded for the fresh samples presented in Figure 3 did not reveal structures like those. For $3NiO_x/CeO_2$, as well as for $5NiO_x/CeO_3$ samples, carbon whiskers of diameters comparable with nickel/nickel oxide grains can be observed. Based on the data from the literature [65], it can be stated that spherical morphology is less favorable for activity than other ones.

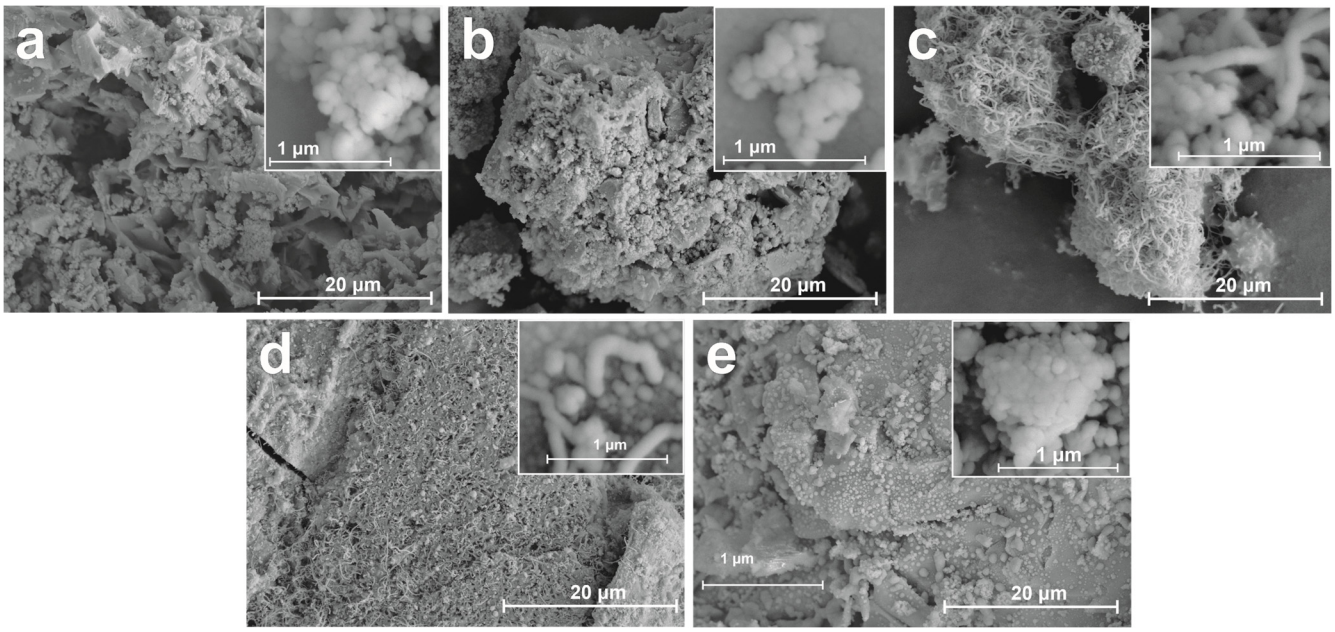

Figure 9. Scanning electron microscopic images of the spent catalysts $0.2NiO_x/CeO_2$ (**a**), $1NiO_x/CeO_2$ (**b**), $3NiO_x/CeO_2$ (**c**), $5NiO_x/CeO_2$ (**d**), and $10NiO_x/CeO_2$ (**e**). The inserts with higher magnification are added for all samples.

4. Conclusions

The described structural and functional investigations of a series of NiO_x/CeO_2 catalysts of various nickel loadings showed that both catalytic activities of our samples as well as their surface properties distinctly depend on nickel concentration. The observed character of this dependence is nonlinear. The metallic to oxidized nickel content ratio as well as the activity of the investigated samples in dry methane reforming initially increased with nickel loading and subsequently tended to decrease after achieving the maximal values for a threshold Ni content of *ca.* 3 wt. %. The determined optimal nickel concentration corresponds to the most effective active centers. However, taking into account the reported results of catalytic stability, a slightly higher loading of nickel (i.e., 5 wt. %) can be more favorable for DMR catalysts, i.e., 5 wt. %. The obtained results showed that the optimization of nickel loading belongs to the crucial and indispensable steps to properly design an active and stable catalyst for dry methane reforming.

Author Contributions: Conceptualization, A.A. and P.L.; methodology, A.A. and P.L.; formal analysis, P.L., M.M. (Mateusz Marzec) and K.S.; investigation, P.L., M.M. (Mateusz Marzec), K.S., M.K. and M.M. (Marek Michalik); resources, A.A.; writing—original draft preparation, P.L.; writing—review and editing, A.A. and P.L.; supervision, A.A.; funding acquisition, A.A. All authors have read and agreed to the published version of the manuscript.

Funding: The research for this publication has been supported by a grant from the Priority Research Area Anthropocene (FP Man–Mind–Environment Hub) under the Strategic Programme Excellence Initiative at the Jagiellonian University.

Data Availability Statement: The data presented in this study are available on request from the corresponding author.

Conflicts of Interest: The authors declare no conflicts of interest.

References

1. Song, C. Global Challenges and Strategies for Control, Conversion and Utilization of CO_2 for Sustainable Development Involving Energy, Catalysis, Adsorption and Chemical Processing. *Catal. Today* **2006**, *115*, 2–32. [CrossRef]
2. Usman, M.; Wan Daud, W.M.A.; Abbas, H.F. Dry Reforming of Methane: Influence of Process Parameters—A Review. *Renew. Sustain. Energy Rev.* **2015**, *45*, 710–744. [CrossRef]
3. Wang, C.; Wang, Y.; Chen, M.; Liang, D.; Yang, Z.; Cheng, W.; Tang, Z.; Wang, J.; Zhang, H. Recent Advances during CH_4 Dry Reforming for Syngas Production: A Mini Review. *Int. J. Hydrogen Energy* **2021**, *46*, 5852–5874. [CrossRef]
4. Fisher, F.; Tropsch, H. Conversion of Methane into Hydrogen and Carbon Monoxide. *Brennst.-Chem.* **1928**, *9*, 39–46.
5. Zhang, G.; Liu, J.; Xu, Y.; Sun, Y. A Review of CH_4–CO_2 Reforming to Synthesis Gas over Ni-Based Catalysts in Recent Years (2010–2017). *Int. J. Hydrogen Energy* **2018**, *43*, 15030–15054. [CrossRef]
6. Arora, S.; Prasad, R. An Overview on Dry Reforming of Methane: Strategies to Reduce Carbonaceous Deactivation of Catalysts. *RSC Adv.* **2016**, *6*, 108668–108688. [CrossRef]
7. Lang, J. Experimentelle Beiträge zur Kenntnis der Vorgänge bei der Wasser- und Heizgasbereitung. *Z. Phys. Chem.* **2017**, *2U*, 161–183. [CrossRef]
8. Aramouni, N.A.K.; Touma, J.G.; Tarboush, B.A.; Zeaiter, J.; Ahmad, M.N. Catalyst Design for Dry Reforming of Methane: Analysis Review. *Renew. Sustain. Energy Rev.* **2018**, *82*, 2570–2585. [CrossRef]
9. Abdulrasheed, A.; Jalil, A.A.; Gambo, Y.; Ibrahim, M.; Hambali, H.U.; Shahul Hamid, M.Y. A Review on Catalyst Development for Dry Reforming of Methane to Syngas: Recent Advances. *Renew. Sustain. Energy Rev.* **2019**, *108*, 175–193. [CrossRef]
10. Guan, Y.; Song, G.; Li, C.; Lim, K.H.; Wang, B.; Xia, L.; Song, H.; Liu, Y.; Wu, C.; Kawi, S. Ni-Based Core-Shell Structured Catalysts for Efficient Conversion of CH_4 to H_2: A Review. *Carbon Capture Sci. Technol.* **2024**, *11*, 100200. [CrossRef]
11. Zhu, H.; Chen, H.; Zhang, M.; Liang, C.; Duan, L. Recent Advances in Promoting Dry Reforming of Methane Using Nickel-Based Catalysts. *Catal. Sci. Technol.* **2024**, *14*, 1712–1729. [CrossRef]
12. Xu, Z.; Park, E.D. Recent Advances in Coke Management for Dry Reforming of Methane over Ni-Based Catalysts. *Catalysts* **2024**, *14*, 176. [CrossRef]
13. Liu, S.; Dun, C.; Jiang, Q.; Xuan, Z.; Yang, F.; Guo, J.; Urban, J.J.; Swihart, M.T. Challenging Thermodynamics: Combining Immiscible Elements in a Single-Phase Nano-Ceramic. *Nat. Commun.* **2024**, *15*, 1167. [CrossRef] [PubMed]
14. Kim, M.J.; Kim, J.; Kim, Y.J.; Youn, J.R.; Kim, D.H.; Shapiro, D.; Guo, J.; Lee, K. Surface Control of Ni-Al_2O_3 Dry Reforming of Methane Catalyst by Composition Segregation. *J. CO2 Util.* **2024**, *81*, 102721. [CrossRef]

15. Bai, X.; Yao, X.; Cheng, Q.; Mohamed, H.O.; Telalovic, S.; Melinte, G.A.; Emwas, A.H.; Gascon, J.; Castaño, P. Engineering the TiO_x Overlayer on Ni Catalyst to Balance Conversion and Stability for Methane Dry-CO_2 Reforming. *ACS Sustain. Chem. Eng.* **2024**, *12*, 633–644. [CrossRef]
16. Kaviani, M.; Rezaei, M.; Alavi, S.M.; Akbari, E. Biogas Dry Reforming over Nickel-Silica Sandwiched Core–Shell Catalysts with Various Shell Thicknesses. *Fuel* **2024**, *355*, 129533. [CrossRef]
17. Al-Fatesh, A.S.; Patel, N.; Srivastava, V.K.; Osman, A.I.; Rooney, D.W.; Fakeeha, A.H.; Abasaeed, A.E.; Alotibi, M.F.; Kumar, R. Iron-Promoted Zirconia-Alumina Supported Ni Catalyst for Highly Efficient and Cost-Effective Hydrogen Production via Dry Reforming of Methane. *J. Environ. Sci.* **2025**, *148*, 274–282. [CrossRef]
18. Elnour, A.Y.; Fakeeha, A.H.; Ibrahim, A.A.; Osman, A.I.; Abasaeed, A.E.; Adil, S.F.; Kumar, R.; Al-Fatesh, A.S. Enhancing Catalytic Performance, Coke Resistance, and Stability with Strontium-Promoted Ni/WO_3-ZrO_2 Catalysts for Methane Dry Reforming. *Res. Chem. Intermed.* **2024**, *50*, 1211–1230. [CrossRef]
19. Abahussain, A.A.M.; Al-Fatesh, A.S.; Singh, S.K.; Almutairi, G.; Fakeeha, A.H.; Ibrahim, A.A.; Abasaeed, A.E.; Frusteri, L.; Labhasetwar, N.K. Cs Promoted Ni/ZrO_2-Al_2O_3 Catalysts for Dry Reforming of Methane: Promotional Effects of Cs for Enhanced Catalytic Activity and Stability. *Arab. J. Chem.* **2024**, *17*, 105564. [CrossRef]
20. Horváth, A.; Németh, M.; Beck, A.; Sáfrán, G.; La Parola, V.; Liotta, L.F.; Žerjav, G.; Roškarič, M.; Pintar, A. Longevity Increase of an Impregnated Ni/CeO_2-Al_2O_3 Dry Reforming Catalyst by Indium. *Appl. Catal. A Gen.* **2024**, *669*, 1167. [CrossRef]
21. Liang, D.; Wang, Y.; Xu, W.; Chen, M.; Wang, M.; Li, C.; Wang, J.; Yang, Z.; Yuan, L. Ni-Pt-Co Clay Catalysts for Dry Reforming of Methane: Influence of Trimetallic Interfaces and Ce Addition. *Mol. Catal.* **2024**, *552*, 113658. [CrossRef]
22. Khatun, R.; Pal, R.S.; Shoeb, M.A.; Khurana, D.; Singhl, S.; Siddiqui, N.; Poddar, M.K.; Khan, T.S.; Bal, R. Generation of Active Oxygen Species by CO_2 Dissociation over Defect-Rich Ni-Pt/CeO_2 Catalyst for Boosting Methane Activation in Low-Temperature Dry Reforming: Experimental and Theoretical Study. *Appl. Catal. B Environ.* **2024**, *340*, 123243. [CrossRef]
23. Fakeeha, A.H.; Bagabas, A.A.; Lanre, M.S.; Osman, A.I.; Kasim, S.O.; Ibrahim, A.A.; Arasheed, R.; Alkhalifa, A.; Elnour, A.Y.; Abasaeed, A.E.; et al. Catalytic Performance of Metal Oxides Promoted Nickel Catalysts Supported on Mesoporous γ-Alumina in Dry Reforming of Methane. *Processes* **2020**, *8*, 522. [CrossRef]
24. Shang, Z.; Li, S.; Li, L.; Liu, G.; Liang, X. Highly Active and Stable Alumina Supported Nickel Nanoparticle Catalysts for Dry Reforming of Methane. *Appl. Catal. B Environ. J.* **2017**, *201*, 302–309. [CrossRef]
25. Bacariza, C.; Karam, L.; El Hassan, N.; Lopes, J.M.; Henriques, C. Carbon Dioxide Reforming of Methane over Nickel-Supported Zeolites: A Screening Study. *Processes* **2022**, *10*, 1331. [CrossRef]
26. Moradi, G.; Khezeli, F.; Hemmati, H. Syngas Production with Dry Reforming of Methane over Ni/ZSM-5 Catalysts. *J. Nat. Gas Sci. Eng.* **2016**, *33*, 657–665. [CrossRef]
27. Muñoz, H.J.; Korili, S.A.; Gil, A. Facile Synthesis of an Ni/$LaAlO_3$—Perovskite via an MOF Gel Precursor for the Dry Reforming of Methane. *Catal. Today* **2024**, *429*, 114487. [CrossRef]
28. Wang, Y.; Li, B.; Xiao, Y.S.; Liu, Z.W. NiO-MgO Prepared by the Complex-Decomposition Method as a Catalyst for Carbon Dioxide Reforming of Methane. *Processes* **2023**, *11*, 596. [CrossRef]
29. Aziz, M.A.A.; Jalil, A.A.; Wongsakulphasatch, S.; Vo, D.V.N. Understanding the Role of Surface Basic Sites of Catalysts in CO_2 Activation in Dry Reforming of Methane: A Short Review. *Catal. Sci. Technol.* **2020**, *10*, 35–45. [CrossRef]
30. Adamski, A.; Legutko, P.; Dziadek, K.; Michalik, M.; Sadykov, V.A. Dry Reforming of Methane on Supported Catalysts Based on Nickel as an Example of Technology Limiting Emission Level of Greenhouse Gases. *Przem. Chem.* **2019**, *98*, 1158–1161. [CrossRef]
31. Adamski, A.; Legutko, P.; Dziadek, K.; Parkhomenko, K.; Aymonier, C.; Sadykov, V.A.; Roger, A.-C. Role of CeO_2-ZrO_2 Support for Structural, Textural and Functional Properties of Ni-Based Catalysts Active in Dry Reforming of Methane. *E3S Web Conf.* **2019**, *108*, 02018. [CrossRef]
32. Auxéméry, A.; Frias, B.B.; Smal, E.; Dziadek, K.; Philippot, G.; Legutko, P.; Simonov, M.; Thomas, S.; Adamski, A.; Sadykov, V.; et al. Continuous Supercritical Solvothermal Preparation of Nanostructured Ceria-Zirconia as Supports for Dry Methane Reforming Catalysts. *J. Supercrit. Fluids* **2020**, *162*, 104855. [CrossRef]
33. Tu, P.H.; Le, D.N.; Dao, T.D.; Tran, Q.T.; Doan, T.C.D.; Shiratori, Y.; Dang, C.M. Paper-Structured Catalyst Containing CeO_2–Ni Flowers for Dry Reforming of Methane. *Int. J. Hydrogen Energy* **2020**, *45*, 18363–18375. [CrossRef]
34. Pizzolitto, C.; Pupulin, E.; Menegazzo, F.; Ghedini, E.; Di Michele, A.; Mattarelli, M.; Cruciani, G.; Signoretto, M. Nickel Based Catalysts for Methane Dry Reforming: Effect of Supports on Catalytic Activity and Stability. *Int. J. Hydrogen Energy* **2019**, *44*, 28065–28076. [CrossRef]
35. Dębek, R.; Motak, M.; Galvez, M.E.; Grzybek, T.; Da Costa, P. Influence of Ce/Zr Molar Ratio on Catalytic Performance of Hydrotalcite-Derived Catalysts at Low Temperature CO_2 Methane Reforming. *Int. J. Hydrogen Energy* **2017**, *42*, 23556–23567. [CrossRef]
36. Liu, H.; Da Costa, P.; Hadj Taief, H.B.; Benzina, M.; Gálvez, M.E. Ceria and Zirconia Modified Natural Clay Based Nickel Catalysts for Dry Reforming of Methane. *Int. J. Hydrogen Energy* **2017**, *42*, 23508–23516. [CrossRef]
37. Lin, K.-H.; Chang, H.-F.; Chang, A.C.-C. Biogas Reforming for Hydrogen Production over Mesoporous $Ni_{2x}Ce_{1-x}O_2$ Catalysts. *Int. J. Hydrogen Energy* **2012**, *37*, 15696–15703. [CrossRef]
38. Lanre, M.S.; Al-Fatesh, A.S.; Fakeeha, A.H.; Kasim, S.O.; Ibrahim, A.A.; Al-Awadi, A.S.; Al-Zahrani, A.A.; Abasaeed, A.E. Catalytic Performance of Lanthanum Promoted Ni/ZrO_2 for Carbon Dioxide Reforming of Methane. *Processes* **2020**, *8*, 1502. [CrossRef]
39. Osojnik Črnivec, I.G.; Djinović, P.; Erjavec, B.; Pintar, A. Effect of Synthesis Parameters on Morphology and Activity of Bimetallic Catalysts in CO_2-CH_4 Reforming. *Chem. Eng. J.* **2012**, *207–208*, 299–307. [CrossRef]

40. Aw, M.S.; Osojnik Črnivec, I.G.; Pintar, A. Toward Enhanced Conversion of Model Biogas Mixtures: Parametric Tuning and Mechanistic Study for Ceria-Zirconia Supported Nickel-Cobalt Catalyst. *Catal. Sci. Technol.* **2014**, *4*, 1340–1349. [CrossRef]
41. Newnham, J.; Mantri, K.; Amin, M.H.; Tardio, J.; Bhargava, S.K. Highly Stable and Active Ni-Mesoporous Alumina Catalysts for Dry Reforming of Methane. *Int. J. Hydrogen Energy* **2012**, *37*, 1454–1464. [CrossRef]
42. Zhang, J.; Wang, H.; Dalai, A.K. Effects of Metal Content on Activity and Stability of Ni-Co Bimetallic Catalysts for CO_2 Reforming of CH_4. *Appl. Catal. A Gen.* **2008**, *339*, 121–129. [CrossRef]
43. Jeong, H.; Kim, K.I.; Kim, D.; Song, I.K. Effect of Promoters in the Methane Reforming with Carbon Dioxide to Synthesis Gas over Ni/HY Catalysts. *J. Mol. Catal. A Chem.* **2006**, *246*, 43–48. [CrossRef]
44. Lee, J.A.; Bae, Y.; Hong, K.; Hong, J. Comparative Evaluation of Ni-Based Bimetallic Catalysts for Dry Reforming of Methane at Low Temperature: The Effect of Alloy Itself on Performance. *Int. J. Energy Res.* **2022**, *46*, 11228–11249. [CrossRef]
45. Abdelsadek, Z.; Köten, H.; Gonzalez-Cortes, S.; Cherifi, O.; Halliche, D.; Masset, P.J. Lanthanum-Promoted Nickel-Based Catalysts for the Dry Reforming of Methane at Low Temperatures. *JOM* **2023**, *75*, 727–738. [CrossRef]
46. Lyu, Y.; Jocz, J.; Xu, R.; Stavitski, E.; Sievers, C. Nickel Speciation and Methane Dry Reforming Performance of $Ni/Ce_xZr_{1-x}O_2$ Prepared by Different Synthesis Methods. *ACS Catal.* **2020**, *10*, 11235–11252. [CrossRef]
47. Scherrer, P. Bestimmung der Größe und der inneren Struktur von Kolloidteilchen mittels Röntgenstrahlen. *Nachrichten Von Der Ges. Der Wiss. Zu Göttingen Math. Kl.* **1918**, *1918*, 98–100.
48. André, R.S.; Zanetti, S.M.; Varela, J.A.; Longo, E. Synthesis by a Chemical Method and Characterization of $CaZrO_3$ Powders: Potential Application as Humidity Sensors. *Ceram. Int.* **2014**, *40*, 16627–16634. [CrossRef]
49. Martín-Espejo, J.L.; Merkouri, L.P.; Gándara-Loe, J.; Odriozola, J.A.; Reina, T.R.; Pastor-Pérez, L. Nickel-Based Cerium Zirconate Inorganic Complex Structures for CO_2 Valorisation via Dry Reforming of Methane. *J. Environ. Sci.* **2024**, *140*, 12–23. [CrossRef]
50. Fakeeha, A.H.; Kasim, S.O.; Ibrahim, A.A.; Abasaeed, A.E.; Al-Fatesh, A.S. Influence of Nature Support on Methane and CO_2 Conversion in a Dry Reforming Reaction over Nickel-Supported Catalysts. *Materials* **2019**, *12*, 1777. [CrossRef]
51. Mo, L.; Fei, J.; Huang, C.; Zheng, X. Reforming of Methane with Oxygen and Carbon Dioxide to Produce Syngas over a Novel $Pt/CoAl_2O_4/Al_2O_3$ Catalyst. *J. Mol. Catal. A Chem.* **2003**, *193*, 177–184. [CrossRef]
52. Yang, M.; Shen, G.; Wang, Q.; Deng, K.; Liu, M.; Chen, Y.; Gong, Y.; Wang, Z. Roles of Oxygen Vacancies of CeO_2 and Mn-Doped CeO2 with the Same Morphology in Benzene Catalytic Oxidation. *Molecules* **2021**, *26*, 6363. [CrossRef] [PubMed]
53. Gómez, D.A.; Coello, J.; Maspoch, S. The Influence of Particle Size on the Intensity and Reproducibility of Raman Spectra of Compacted Samples. *Vib. Spectrosc.* **2019**, *100*, 48–56. [CrossRef]
54. Chen, K.; Zhang, T.; Chen, X.; He, Y.; Liang, X. Model Construction of Micro-Pores in Shale: A Case Study of Silurian Longmaxi Formation Shale in Dianqianbei Area, SW China. *Pet. Explor. Dev.* **2018**, *45*, 412–421. [CrossRef]
55. Saw, E.T.; Oemar, U.; Ang, M.L.; Kus, H.; Kawi, S. High-Temperature Water Gas Shift Reaction on $Ni–Cu/CeO_2$ Catalysts: Effect of Ceria Nanocrystal Size on Carboxylate Formation. *Catal. Sci. Technol.* **2016**, *6*, 5336–5349. [CrossRef]
56. Natile, M.M.; Boccaletti, G.; Glisenti, A. Properties and Reactivity of Nanostructured CeO_2 Powders: Comparison among Two Synthesis Procedures. *Chem. Mater.* **2005**, *17*, 6272–6286. [CrossRef]
57. Chen, K.; Li, W.; Guo, G.; Zhu, C.; Wu, W.; Yuan, L. Nickel Hydroxide Nanosheets Prepared by a Direct Manual Grinding Strategy for High-Efficiency Catalytic Combustion of Methane. *ACS Omega* **2022**, *7*, 8536–8546. [CrossRef] [PubMed]
58. Bensalem, A.; Muller, J.C.; Bozon-Verduraz, F. Faraday Communications. From Bulk CeO_2 to Supported Cerium–Oxygen Clusters: A Diffuse Reflectance Approach. *J. Chem. Soc. Faraday Trans.* **1992**, *88*, 153–154. [CrossRef]
59. Guo, M.; Lu, J.; Wu, Y.; Wang, Y.; Luo, M. UV and Visible Raman Studies of Oxygen Vacancies in Rare-Earth-Doped Ceria. *Langmuir* **2011**, *27*, 3872–3877. [CrossRef]
60. Kambolis, A.; Matralis, H.; Trovarelli, A.; Papadopoulou, C. Ni/CeO_2-ZrO_2 Catalysts for the Dry Reforming of Methane. *Appl. Catal. A Gen.* **2010**, *377*, 16–26. [CrossRef]
61. Biesinger, M.C.; Payne, B.P.; Lau, L.W.M.; Gerson, A.; Smart, R.S.C. X-ray Photoelectron Spectroscopic Chemical State Quantification of Mixed Nickel Metal, Oxide and Hydroxide Systems. *Surf. Interface Anal.* **2009**, *41*, 324–332. [CrossRef]
62. Babakouhi, R.; Alavi, S.M.; Rezaei, M.; Akbari, E.; Varbar, M. Combined CO_2 Reforming and Partial Oxidation of Methane over Mesoporous Nanostructured $Ni/M\text{-}Al_2O_3$ Catalyst: Effect of Various Support Promoters and Nickel Loadings. *J. CO2 Util.* **2023**, *70*, 102427. [CrossRef]
63. Dedov, A.G.; Loktev, A.S.; Arkhipova, V.A.; Bykov, M.A.; Sadovnikov, A.A.; Cherednichenko, K.A.; Shandryuk, G.A. A New Approach to the Preparation of Stable Oxide-Composite Cobalt–Samarium Catalysts for the Production of Hydrogen by Dry Reforming of Methane. *Processes* **2023**, *11*, 2296. [CrossRef]
64. Shtyka, O.; Zakrzewski, M.; Ciesielski, R.; Kedziora, A.; Dubkov, S.; Ryazanov, R.; Szynkowska, M.; Maniecki, T. Efficient Removal of the Carbon Deposits Formed during the Mixed Methane Reforming over Ni/Al_2O_3. *Korean J. Chem. Eng.* **2020**, *37*, 209–215. [CrossRef]
65. Stanley, K.; Kelly, S.; Sullivan, J.A. Effect of Ni NP Morphology on Catalyst Performance in Non-Thermal Plasma-Assisted Dry Reforming of Methane. *Appl. Catal. B Environ.* **2023**, *328*, 122533. [CrossRef]